

Surgical Scene Segmentation using a Spike-Driven Video Transformer with Real-Time Potential

Shihao Zou, Jingjing Li, Wei Ji, Jincai Huang, Kai Wang, Guo Dan, Weixin Si, Yi Pan

Abstract—Modern surgical systems increasingly rely on intelligent scene understanding to provide timely situational awareness for enhanced intra-operative safety. Within this pipeline, surgical scene segmentation plays a central role in accurately perceiving operative events. Although recent deep learning models, particularly large-scale foundation models, achieve remarkable segmentation accuracy, their substantial computational demands and power consumption hinder real-time deployment in resource-constrained surgical environments. To address this limitation, we explore the emerging spiking neural networks (SNN) as a promising paradigm for highly efficient surgical intelligence. By mimicking the brain’s neural dynamics and communicating through binary 0/1 spikes, SNNs achieve feed-forward computation with addition-only operations, offering inherent advantages in energy efficiency. However, their performance is still constrained by the scarcity of labeled surgical data and the inherently sparse nature of surgical video representations. To this end, we propose *SpikeSurgSeg*, the first spike-driven video Transformer framework tailored for surgical scene segmentation with real-time potential on non-GPU platforms. To address the limited availability of surgical annotations, we introduce a surgical-scene masked autoencoding pretraining strategy for SNNs that enables robust spatiotemporal representation learning via layer-wise tube masking. Building on this pretrained backbone, we further adopt a lightweight spike-driven segmentation head that produces temporally consistent predictions while preserving the low-latency characteristics of SNNs. Extensive experiments on EndoVis18 and our in-house SurgBleed dataset demonstrate that *SpikeSurgSeg* achieves mIoU comparable to state-of-the-art (SOTA) Artificial Neural Networks (ANN)-based models while reducing inference latency by at least 8×. Notably, it delivers over 20× acceleration relative to most foundation-model baselines, underscoring its potential for time-critical surgical scene segmentation.

Index Terms—Surgical Scene Segmentation, Spiking Neural Networks, Masked Visual Modeling

I. INTRODUCTION

Modern surgery has transformed from an experience-driven art into a data-centric, technology-augmented discipline, propelled by the convergence of advanced imaging systems,

S. Zou is with Shenzhen Institutes of Advanced Technology, Chinese Academy of Sciences, Shenzhen, China. (E-mail: sh.zou@siat.ac.cn)

J. Li is with University of Alberta, Edmonton, Canada. (E-mail: jingjin1@ualberta.ca)

W. Ji is with School of Medicine, Yale University, New Haven, US. (E-mail: wei.ji@yale.edu)

J. Huang is with Southern University of Science and Technology, jointly with Shenzhen University of Advanced Technology, Shenzhen, China. (E-mail: 12533480@mail.sustech.edu.cn)

K. Wang is with Nanfang Hospital Southern Medical University, Guangzhou, China. (E-mail: kaiwangsmu@163.com)

G. Dan is with School of Biomedical Engineering, Shenzhen University, Shenzhen, China. (E-mail: danguo@szu.edu.cn)

W. Si and Y. Pan are with Faculty of Computer Science and Control Engineering, Shenzhen University of Advanced Technology, Shenzhen, China. (E-mail: panyi@suat-sz.edu.cn, siweixin@suat-sz.edu.cn)

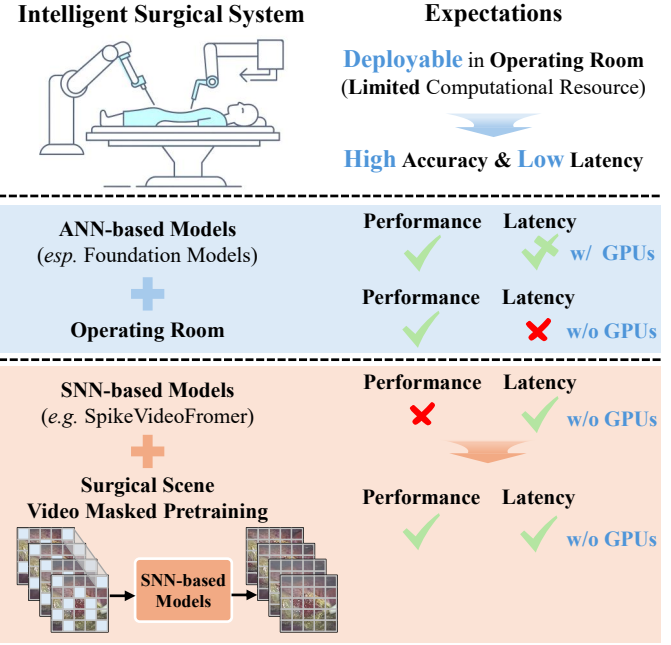


Fig. 1: Motivation of Our Work. Intelligent surgical systems should achieve both high accuracy and low latency to be deployable in the operating room. Although *ANN-based models*, especially foundation models, deliver strong performance for surgical scene segmentation, they rely on power-hungry GPUs to maintain low latency, which is impractical under the physical and safety constraints of surgical environments. In contrast, emerging *SNN-based models* offer inherent efficiency but often suffer from performance degradation due to their sparse spike representations. To overcome this limitation, we propose a surgical-scene masked pretraining strategy that enhances surgical scene segmentation performance of SNNs while retaining their low-latency advantage.

robotic platforms, and multimodal intra-operative sensing technologies [1]–[4]. These innovations have produced massive streams of heterogeneous surgical data, such as high-resolution surgical or endoscopic videos, laying the foundation for computational models to perceive and interpret surgical scenes. Within this paradigm, surgical scene segmentation has emerged as a fundamental component, aiming to comprehensively recognize and contextualize instruments, anatomical structures, and operative states [5]–[8].

Despite notable progress, surgical scene segmentation still faces significant obstacles to clinical deployment. Deep learning models, especially large foundation models with hundreds of millions of parameters, demand substantial computational

power and energy, making real-time execution in the operating room impractical [8] (Fig. 1). These limitations are further amplified by the physical and safety constraints of surgical environments, *i.e.*, restricted space, strict heat dissipation limits, and tight power budgets, all of which prohibit the integration of high-end GPU clusters. Conversely, CPU-only or embedded platforms, while more realistic for clinical use, often incur prohibitively high latency. Consequently, a persistent gap remains between research prototypes and deployable intelligent surgical systems: current deep learning models struggle to deliver both high accuracy and low latency under energy-constrained hardware, hindering seamless adoption in real-world intra-operative environments [9].

To bridge this gap, we explore brain-inspired computing as a promising paradigm for building efficient and intelligent surgical systems. Within this paradigm, SNNs stand out for their exceptional energy efficiency, achieved by mimicking the temporal coding and asynchronous spike communication of brain neurons [10], [11]. In contrast to conventional ANNs that rely heavily on dense floating-point multiplications, SNNs transmit information through discrete 0/1 spikes and perform feed-forward computations upon spike occurrence with addition-only operations, thereby substantially reducing power consumption. Furthermore, the intrinsic temporal dynamics of SNNs naturally align with the sequential structure of surgical videos, making them both a biologically plausible and computationally efficient alternative for real-time surgical scene segmentation.

Although SNNs have demonstrated performance comparable to ANNs in image classification [12]–[14], object detection [15], [16], and semantic segmentation [17]–[20], their application to surgical scene segmentation remains largely unexplored. Two key challenges hinder their adoption in this domain. 1) Unlike the abundance of large-scale natural image and video datasets, annotated surgical datasets are scarce, limiting effective representation learning for SNN-based models. 2) Most existing SNN architectures have been developed and validated on generic image benchmarks, leaving it unclear whether they can adequately capture the complex, domain-specific characteristics required for accurate surgical scene segmentation. Addressing these challenges is essential to promote the efficiency advantages of SNNs while maintaining high accuracy in time-critical clinical environments.

In this paper, we propose *SpikeSurgSeg*, the first spike-driven video Transformer framework tailored for surgical scene segmentation with real-time potential under non-GPU settings. At its core is a spike-driven video Transformer as the encoder that enables efficient spatiotemporal modeling with linear space-time computational complexity. To address the scarcity of labeled surgical data, we first pretrain the SNN-based encoder using a tailored surgical-scene masked autoencoding strategy, enabling it to learn robust visual and temporal representations from unlabeled surgical videos before downstream fine-tuning. This pretraining employs layer-wise tube masking across spatial and temporal dimensions, guiding the SNN encoder to reconstruct masked regions and internalize motion-aware contextual priors. To further enhance semantic understanding, we incorporate semantic knowledge distillation

from SAM2 [21], aligning the sparse spike representations of the SNN with the dense feature space of a strong vision foundation model. This injects global semantic priors into the spike-driven domain and complements the encoder’s sparse spatiotemporal representations. Following masked video pre-training, the SNN-based encoder is paired with a lightweight spike-driven segmentation head that integrates a spike pyramid and a memory readout module. This design ensures temporally consistent video segmentation while preserving the inherent low-latency and low-energy benefits of spike-driven inference.

Our main contributions are summarized as follows:

- We propose *SpikeSurgSeg*, the first SNN-based framework designed specifically for surgical scene segmentation. By leveraging spike-driven brain-inspired computation, the framework achieves energy-efficient, semantically enriched, and real-time-capable segmentation under non-GPU settings, representing a significant step toward deployable intelligent surgical systems.
- We introduce a tailored surgical-scene masked autoencoding pretraining strategy for the SNN-based video encoder. By applying layer-wise tube masking across spatial and temporal dimensions, it enables robust spatiotemporal representation learning and effectively alleviates the challenge of limited labeled surgical data, thereby improving performance on downstream surgical segmentation tasks.
- We demonstrate that our SNN-based approach attains mIoU comparable to SOTA ANN baselines while achieving *at least 8× faster inference* and *5.1× lower energy consumption* on both the EndoVis18 dataset and our in-house SurgBleed dataset. Notably, the model achieves *over 20× acceleration* compared with most foundation-model baselines.

II. RELATED WORK

Spiking Neural Networks (SNNs) are a brain-inspired learning framework where spiking neurons emulate the communication mechanism of the mammalian visual cortex [10], [11]. Unlike ANNs that rely heavily on floating-point multiplications for signal propagation, SNNs mimic the brain’s neural dynamics through binary (0/1) spike-based communication. This spike-driven process allows information to propagate using simple additions while ignoring inactive (non-spiking) connections, resulting in significantly improved computational efficiency compared to traditional ANNs. However, training SNNs at scale remains a significant challenge due to the non-differentiable nature of spike generation. To address this, early efforts focused on converting trained ANNs into SNNs [22], achieving strong results in simple classification tasks but falling short in more complex vision problems. In contrast, direct training methods leverage back-propagation through time (BPTT) with surrogate gradients to approximate the derivative of the spiking function [23], [24], enabling the design of increasingly sophisticated SNN architectures as follows.

Convolution-based SNNs seek to deepen and enhance the representational capacity of spiking networks by adopting architectural elements from deep CNNs. Models like SEW-SNNs [12] and MS-SNNs [25] mitigate issues like vanishing

gradients and disrupted identity mappings through spike- or membrane-level residual connections. Despite their strong performance on classical image recognition task, these convolutional SNNs still show limited competitiveness on more complex large-scale vision tasks.

Transformer-based SNNs represent a major advancement in the design of SNNs. Early work [13] introduces multi-dimensional attention in Spiking Transformers, achieving promising results on large-scale image recognition, albeit at the cost of efficiency due to reliance on real-valued membrane potentials. To address this, subsequent studies [26], [27] developed spike-driven self-attention mechanisms based on dot-product similarity between binary spike tensors. By removing the softmax function and reordering the computation of queries, keys, and values, these models attain linear complexity with respect to token length. Building on this, SpikeFormer V2 [14] incorporates a hybrid architecture combining Convolution and Transformer-based SNNs, improving feature encoding over pure ViT-like designs [28]. Further progress includes masked self-supervised training for spike-driven models [29], enhancing their representation learning on downstream image-based tasks. The most recent advancement [20] proposes Hamming attention as a more theoretically grounded spike-driven alternative to standard dot-product attention [30], strengthening the foundation of spike-driven Transformers.

SNNs in Vision Tasks have shown growing potential as energy-efficient alternatives to ANNs, demonstrating competitive performance across a variety of challenging tasks, including large-scale image classification [12]–[14], semantic segmentation [17]–[19], and object detection [15], [16]. Most recently, SpikeVideoFormer [20] has extended spike-driven Transformers to video understanding tasks, including classification, pose tracking, and video segmentation. It introduces a spike-driven spatiotemporal attention mechanism featuring linear computational complexity.

Masked Visual Modeling (MVM) is a premier paradigm for self-supervised learning (SSL) in vision, especially in Transformer architectures. The foundational MAE [31] framework introduces masked token prediction for images, learning via reconstructing heavily masked input patches. Its video extensions, *i.e.*, VideoMAE [32] and MAE-ST [32], show that random spacetime masking enables effective spatiotemporal representation learning, with large speedups and performance surpassing supervised alternatives. While MAE targets pixel reconstruction, more recent approaches like MaskFeat [33] predict richer features, specifically HOG descriptors, yielding strong performance in video understanding tasks and generalizing well to images. MCMAE [34] expands this framework by integrating masked convolutions into a hybrid convolution-Transformer architecture and supervising multi-scale features, leading to clear performance gains on classification and detection. Meanwhile, SparK [35] makes MVM viable for pure convolutional backbones, addressing masking irregularities with sparse conv encoders and UNet-style hierarchical decoders, showing solid improvements on detection and segmentation. SdAE [36] employs a student–teacher masked autoencoder with multi-view masking, improving downstream tasks such as segmentation and detection competitively and

efficiently. In the domain of large-scale self-supervision, DINov2 [37] shows that ViTs with discriminative-style SSL, trained on a massive curated dataset, can rival weakly-supervised models—yielding robust, general-purpose visual representations without reconstruction targets. In domain-specific applications, CSMAE [38] tailors masking to the spatiotemporal importance in surgical video frames, pretraining on cataract surgery data and achieving superior step recognition compared to generic pretraining strategies.

Surgical Scene Segmentation is a fundamental task in surgical scene understanding. Early approaches [5], [39], primarily based on CNNs and Transformers, focused on improving performance by incorporating spatial attention, optical flow, and motion priors. These methods gradually evolved from static-frame segmentation toward more sophisticated techniques that leverage intra- and inter-video relationships and contrastive learning. Building on the success of foundation models in natural image or video segmentation, *e.g.*, SAM [40] and SAM2 [21], recent research has explored their adaptation to medical image segmentation. MedSAM [41] develops a universal medical segmentation model based on SAM, trained on a large-scale medical image dataset. Other efforts [42] finetune vision-language models for text-promptable surgical scene segmentation. More recent works [6], [43], [44] propose efficient tuning strategies to incorporate surgical-specific knowledge, such as 3D medical images or surgical videos, into SAM for improving generalization. SurgicalSAM2 [7] extends by finetuning SAM2 with a frame pruning mechanism, further enhancing speed toward real-time GPU deployment.

As highlighted by [8], real-time performance is crucial for translating intelligent surgical systems into clinical practice. Yet most existing methods rely on ANNs, particularly large foundation models, which incur high computational costs and limit practical deployment. In contrast, we explore brain-inspired SNNs for ultra-efficient and temporally aware segmentation. Unlike CNN- or ViT-based architectures, our model leverages asynchronous spike-driven dynamics to achieve significant gains in energy efficiency and inference latency. Moreover, the proposed spike-driven video transformer encodes spatiotemporal context through MVM-inspired SSL, effectively capturing the unique dynamics of surgical scenes to enable real-time surgical video analysis.

III. METHOD

A. Spiking Neural Networks Revisit

Spiking Neuron Model is the fundamental difference between the ANNs and SNNs. The *leaky integrate-and-fire (LIF) neuron* is a widely used computational unit in SNNs. The LIF neuron maintains a membrane potential $u_{[t]}$, decay through time with a leaky constant β . The potential will be updated upon receiving input spike trains $X_{[t]}$ from its connected neurons over T time steps. When the potential surpasses the threshold V_{th} at time t , the neuron will emit a spike $S_{[t]}$ and undergoes a soft reset [26] by reducing its potential by u_{th} . The dynamics can be expressed as

$$\begin{aligned} H_{[t]} &= \beta U_{[t-1]} + X_{[t]}, \\ S_{[t]} &= \Theta(H_{[t]} - u_{\text{th}}), \quad U_{[t]} = H_{[t]} - u_{\text{th}} S_{[t]}, \end{aligned} \quad (1)$$

where Θ is the element-wise Heaviside step function:

$$\Theta(H_{[t]} - u_{\text{th}}) = \begin{cases} 1, & \text{if } H_{[t]} \geq u_{\text{th}} \\ 0, & \text{otherwise} \end{cases}.$$

For convenience, we denote the temporal spiking process of LIF neuron as $\mathcal{SN}_s(U)$ with scaled threshold $s \cdot u_{\text{th}}$.

Feedforward Process in SNNs normally consists of stacked layers of spiking neurons. For the l -th layer with $N^{(l)}$ neurons, we denote the membrane potentials and spike outputs at time t as vectors $\mathbf{U}_{[t]}^{(l)} \in \mathbb{R}^{N^{(l)}}$ and $\mathbf{S}_{[t]}^{(l)} \in \{0, 1\}^{N^{(l)}}$, respectively. The synaptic weights between layers $l-1$ and l are represented by $\mathbf{W}^{(l)} \in \mathbb{R}^{N^{(l-1)} \times N^{(l)}}$. Thus, the feedforward process is defined as

$$\begin{aligned} \mathbf{H}_{[t]}^{(l)} &= \underbrace{\beta \mathbf{U}_{[t-1]}^{(l)}}_{\text{leak}} + \underbrace{\mathbf{W}^{(l)} \mathbf{S}_{[t]}^{(l-1)}}_{\text{charge}}, \\ \mathbf{S}_{[t]}^{(l)} &= \underbrace{\Theta(\mathbf{H}_{[t]}^{(l)} - u_{\text{th}})}_{\text{spike}}, \quad \mathbf{U}_{[t]}^{(l)} = \mathbf{H}_{[t]}^{(l)} - \underbrace{u_{\text{th}} \mathbf{S}_{[t]}^{(l)}}_{\text{reset}}. \end{aligned} \quad (2)$$

Computational Complexity and Energy Consumption are primarily determined by two key factors that contribute to the efficiency of SNNs as follow:

- 1) Unlike ANNs, which rely on costly matrix multiplications during feedforward computation, SNNs *replace these operations with simple additions*. This is possible because the spike vector $\mathbf{S}_{[t]}^{(l-1)}$ is binary, making the computation of $\mathbf{W}^{(l)} \mathbf{S}_{[t]}^{(l-1)}$ in Eq.(2) much more energy-efficient. As a result, SNNs exhibit lower power consumption and latency on neuromorphic hardware [10], [45], compared to ANNs, which achieve high throughput on GPUs at the cost of significantly higher energy. Specifically, in 45nm CMOS technology [46], a 32-bit floating-point multiply-and-accumulate (MAC) operation in ANNs consumes $E_{\text{MAC}} = 4.6pJ$, while a simple accumulate (AC) operation in SNNs requires only $E_{\text{AC}} = 0.9pJ$, a $5.1 \times$ energy reduction. Similarly, on the AMD Xilinx ZCU104 platform [47], SNNs achieve 5529.6 AC GFLOPs per second, compared to 691.2 MAC GFLOPs for ANNs, an $8 \times$ speedup.
- 2) *SNNs also benefit from sparse activation.* Because most entries in $\mathbf{S}_{[t]}^{(l-1)}$ are zero, most multiplications in $\mathbf{W}^{(l)} \mathbf{S}_{[t]}^{(l-1)}$ can be skipped, substantially reducing computation. Assuming a spiking rate of ρ (typically $\tilde{20}\%$) over T time steps in the l -th layer, the computational complexity decreases from $\mathcal{O}(TN^{(l-1)}N^{(l)})$ for ANNs to $\mathcal{O}(\rho TN^{(l-1)}N^{(l)})$, yielding a $\rho \times$ reduction in computations.

Training SNNs are typically trained using backpropagation through time (BPTT) [23], [48], where the non-differentiable Heaviside step function is approximated by a surrogate gradient. Following the formulation in [12], we adopt the ATan surrogate gradient function in this work.

Recent studies [16], [19] also introduce the *Integer Integrate-and-Fire neuron* (IntIF), which enhances the performance of SNNs on complex vision tasks while incurring minimal additional computational cost. Unlike LIF neurons

that produce binary 0/1 outputs, IntIF neurons output integer-valued spikes. Specifically, an IntIF neuron with integer setting Z generates spike outputs within the range $S_{[t]} \in \{0, 1, \dots, Z-1\}$. While the training process of IntIF-based models still follows BPTT, the inference process can be unfolded into Z sub-steps of 0/1 spikes. In each sub-step, the charge term in Eq. (2) still involves only additions, avoiding any multiplications. This IntIF configuration is also adopted in our work to further improve model efficiency and performance.

B. Spike-Driven Video Encoder

Spike-Driven Encoder takes a video clip $\mathbf{I} \in \mathbb{R}^{T \times H \times W \times 3}$ as the input. The clip is first transformed into spiking features through temporal spiking. These features are then sequentially processed by two spike-driven CNN blocks followed by two spike-driven Spatiotemporal Transformer blocks. Downsampling modules are inserted between blocks to progressively reduce spatial resolution. At the l -th intermediate layer where $l \in \{0, 1, \dots, 4\}$, the spatial token length corresponds to the flattened spatial dimension, *i.e.*, $N = \frac{H}{2^l} \cdot \frac{W}{2^l}$. The final output feature maps $\mathbf{U}_{\text{latent}} \in \mathbb{R}^{T \times \frac{H}{16} \times \frac{W}{16} \times 12C}$, where C is a tunable hyperparameter that controls the model size.

We adopt SpikeVideoFormer [20] as the backbone of our SNN-based encoder. This architecture follows a *Conv+ViT* design, a paradigm known for strong scalability and generalization in both ANNs [49] and SNNs [14]. As illustrated in Fig. 2 and detailed in Supplementary A, the encoder combines spike-driven CNN blocks that efficiently extract local spatial features with spike-driven spatiotemporal Transformer blocks that capture global dependencies with linear space-time computational complexity through multiplication-free attention. This hybrid design unifies the strengths of hierarchical convolutional modeling and global attention while preserving the addition-only, low-latency computation inherent to SNNs, making the encoder highly suitable for real-time surgical scene segmentation on resource-constrained hardware.

Backbone Variations depends on the channel capacity. In this work, we propose a compact version with $C = 32$ and a larger counterpart with $C = 64$, yielding 16.0M and 56.3M parameters, respectively. Both encoders are initially trained on the ImageNet1K dataset to leverage rich visual features from natural images. These pretrained weights then serve as initialization for subsequent stages, including surgical scene pretraining and downstream segmentation finetuning. The architecture details are provided in Supplementary A.

C. Surgical Scene MAE Pretraining

Self-supervised pretraining has shown remarkable success in ANN-based visual foundation models [31], [32], [34], [35], [38], [50], where the learned representations often outperform those from direct task-specific supervised learning. This paradigm is particularly advantageous for surgical scene understanding, where surgical data with annotations are scarce and expensive. By leveraging MAE pretraining, the model can uncover intrinsic spatial layouts of anatomical structures and surgical instruments, as well as temporal dynamics reflecting

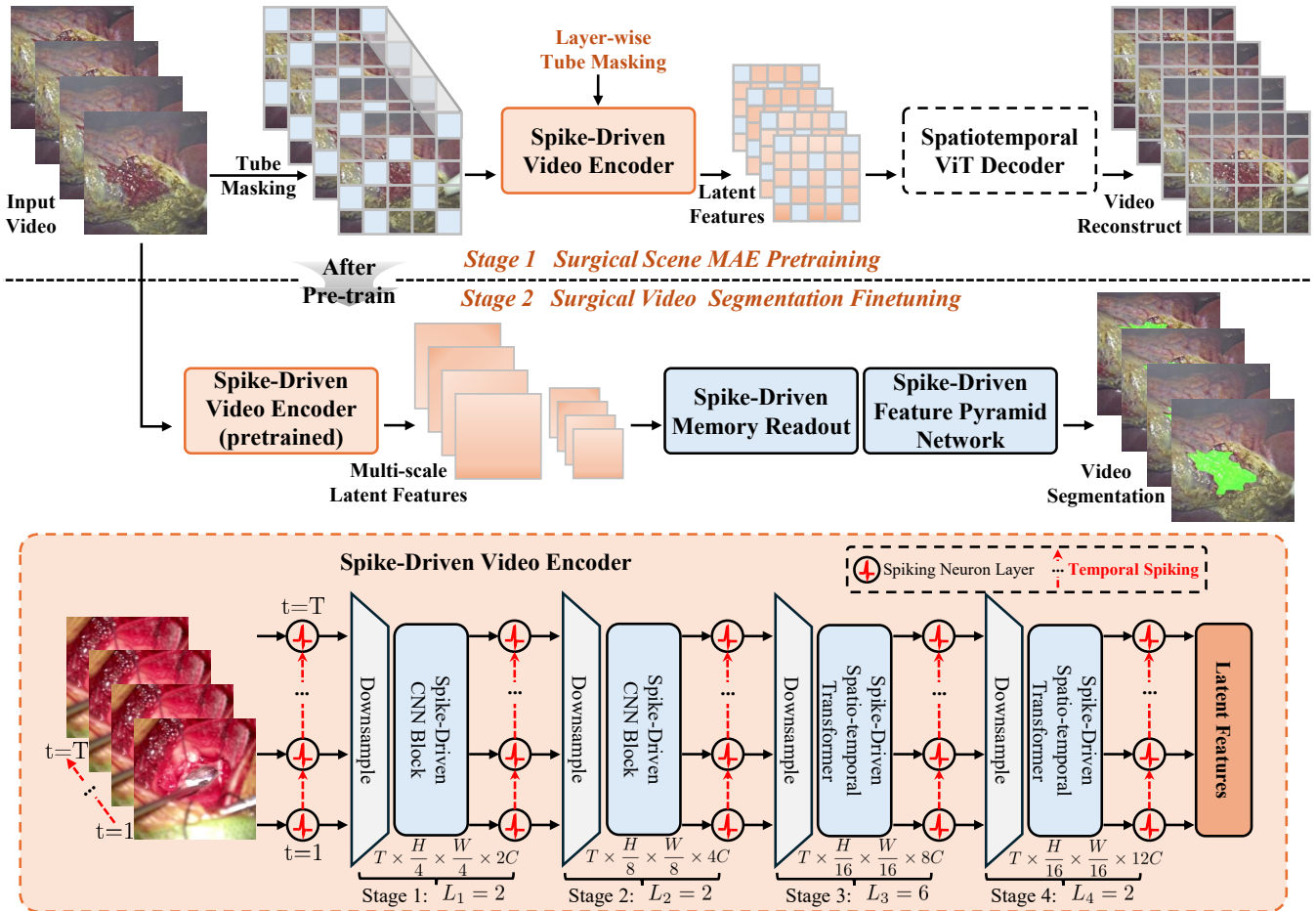


Fig. 2: **SpikeSurgSeg Pipeline.** 1) *Stage 1*: Spike-driven video encoder is pretrained on surgical videos using a masked autoencoding strategy, where a layer-wise tube masking is applied to the input video clip. The masked patches are then reconstructed by aggregating information from unmasked regions. 2) *Stage 2*: Spike-driven memory readout and feature pyramid network are integrated with the spike video encoder, and then the entire SNN-based model is finetuned for the downstream surgical scene segmentation task. The bottom block shows the detailed architecture of the encoder, which employs two spike-driven CNN blocks and two spike-driven spatiotemporal Transformers featuring linear space–time computational complexity.

procedural flow and tool–tissue interactions, thereby enabling robust generalization across downstream surgical tasks.

While video MAE has been well-studied in ANNs, its potential in the context of SNNs remains largely underexplored. Existing work [29] has only considered masked image pre-training for SNNs, without extending to video, which limits the generalization of SNN-based models for complex video tasks. In this work, we introduce a video MAE-style pre-training strategy tailored for spike-driven video encoder. Our method enables SNNs to learn more expressive spatiotemporal features while maintaining their inherent energy efficiency.

Layer-Wise Tube Masking. Given that the encoder outputs spiking features of size $T \times \frac{H}{16} \times \frac{W}{16}$, we first generate corresponding 2D random masking map of shape $\frac{H}{16} \times \frac{W}{16}$ with a masking ratio α . To provide the tube masking map for the l -th layer, this 2D mask is repeated along the temporal dimension T and spatially expanded to cover patches of $2^{4-l} \times 2^{4-l}$ pixels. The resulting layer-wise tube masking map, $M_l \in \{0, 1\}^{T \times \frac{H}{2^l} \times \frac{W}{2^l}}$, is thus aligned with the spatial resolution of each intermediate feature map. As shown in Fig. 3, the mask is applied to the feature maps before

the temporal spiking process, ensuring that masked regions generate no spike activity. This hierarchical masking strategy mitigates distribution shifts and prevents information leakage that can arise when convolution or attention operations are applied directly to partially masked inputs [29], [35].

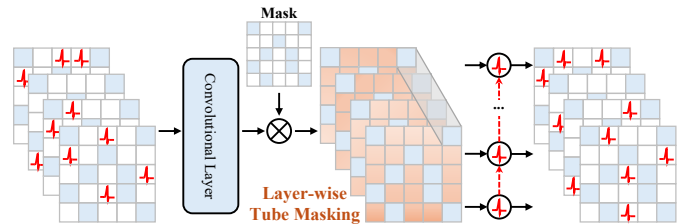


Fig. 3: **Layer-wise Tube Masking.** The tube-shaped mask is applied at each encoder layer to prevent any spike generation within the masked areas, ensuring that no spatial or temporal information leaks into the reconstruction process.

Encoding. The input video clip is first masked by the initial tube mask $M_0 \cdot \mathbf{I}$ and then fed into the spike-driven video encoder. At the l -th layer, outputs from all basic modules

are further modulated by the corresponding layer-wise tube mask M_l . Therefore, the multi-scale latent features extracted by the spike-driven encoder are represented as $[U_1, \dots, U_4]$. The process can be summarized as

$$[U_1, \dots, U_4] = \text{SpikeEncoder}(\mathbf{I}, [M_0, \dots, M_3]). \quad (3)$$

Unlike ViT-based encoders that convert frames into token sequences [32], [50], CNNs preserve spatial relationships during feature encoding, enabling stronger representation learning in the masked pretraining setting.

Decoding. Since our goal is to pretrain an SNN-based encoder for downstream tasks, we adopt a standard ViT [28] as the decoder for simplicity. During pretraining, masked regions in the encoder's output are filled with a learnable mask embedding \mathbf{m} , after which the combined features are flattened, augmented with positional embeddings, and fed into the ViT decoder. The decoder then reconstructs the video clip $\hat{\mathbf{I}}$ following the unflattening operation, formulated as

$$\hat{\mathbf{I}} = \text{ViT-Decoder}(\mathbf{M}_4 \cdot \mathbf{U}_4 + (\mathbf{1} - \mathbf{M}_4) \cdot \mathbf{m}). \quad (4)$$

After pretraining, *the ViT decoder is discarded*, and only the spike-driven encoder is retained for downstream applications.

Training. The loss for pretraining consists of two parts. Let $\Omega = \{i \mid M_4^{(i)} = 0\}$ denote the set of masked pixel indices. The reconstruct loss is the mean squared error (MSE) over these masked regions, formulated as

$$\mathcal{L}_{\text{pretrain}} = \frac{1}{|\Omega|} \sum_{i \in \Omega} \|\mathbf{I}^{(i)} - \hat{\mathbf{I}}^{(i)}\|^2, \quad (5)$$

where i represents the index of pixel values and $|\Omega|$ denotes the total number of masked pixels.

To further enhance visual representation learning of SNN-based models in surgical scenes, we leverage the strong semantic encoding capability of SAM2 [21] via knowledge distillation. A key challenge lies in the representational gap between membrane potential-based features from our spike-driven encoder and activation-based features from the SAM2 encoder, which hinders direct knowledge transfer. To bridge this gap, we introduce a convolutional adapter to align their feature spaces, defined as

$$\mathcal{L}_{\text{kd}} = \|\mathbf{U}_4 - \text{Conv}(\mathbf{U}_{\text{sam}})\|^2, \quad (6)$$

where \mathbf{U}_4 denotes features from the spike-driven encoder and \mathbf{U}_{sam} those from the SAM2 encoder. Similarly, *the adapter is discarded after pretraining*, allowing \mathcal{L}_{kd} to provide semantic supervision from pretrained models while preserving the intrinsic spiking dynamics of spike-driven video encoder.

D. Surgical Video Segmentation Finetuning

After pretraining on surgical scenes, the spike-driven encoder has learned to capture surgical semantic relationships among visual features. Building on this foundation, we initialize our model with the pretrained encoder and attach an additional spike-driven video segmentation head. The entire model is then finetuned end-to-end for this downstream task.

Video Segmentation Head. To highlight the real-time potential of our SNN model for surgical scene segmentation, we

avoid overly complex architectures, focusing instead on validating the effectiveness and efficiency of proposed approach. The segmentation head comprises two main components: 1) Memory Read and Fusion Module: Inspired by [51], semantic features from previous frames (memory) are retrieved and fused with the current frame's features using spike-driven Hamming attention as detailed in Supplementary A, enabling temporal dependency modeling while preserving the event-driven efficiency of SNNs. 2) Spike-Driven Feature Pyramid Networks (SpikeFPN): To maintain computational efficiency, we adapt the standard FPN [52] into a spike-driven design. Starting from the lowest-level feature $\mathbf{O}_4 = \text{Conv}(\mathcal{SN}(\mathbf{U}_4))$, the pyramid aggregation is computed as

$$\mathbf{O}_l = \text{Conv}(\mathcal{SN}(\mathbf{U}_l)) + \text{Upsample}(\mathbf{O}_{l+1}), \quad l \in \{3, 2, 1\}.$$

The multi-scale features are then upsampled and aggregated to produce the logits for the final pixel-wise segmentation prediction, expressed as

$$\hat{\mathbf{y}} = \sum_{l=1}^4 \text{Upsample}(\text{Conv}(\mathcal{SN}(\mathbf{O}_l))). \quad (7)$$

In contrast to prior SNN-based approaches [17], [18] that focus exclusively on single-frame semantic segmentation, our method exploits the inherent spatiotemporal modeling capability of SNNs to perform video segmentation, extending their applicability to real-time surgical video processing.

Training. To finetune the model for surgical video segmentation, we employ a combination of cross-entropy loss and focal loss to mitigate the severe class imbalance commonly observed in surgical datasets. Let \mathbf{y} denote the one-hot representation of the ground-truth semantic label map. The losses are then defined as

$$\mathcal{L}_{\text{CE}} = -\frac{1}{HW} \sum_{i,j} \sum_{k=0}^{H,W} \mathbf{y}_{ijk} \log(\hat{\mathbf{y}}_{ijk}), \quad (8)$$

$$\mathcal{L}_{\text{Focal}} = -\frac{1}{HW} \sum_{i,j} \sum_{k=0}^{H,W} \mathbf{y}_{ijk} (1 - \hat{\mathbf{y}}_{ijk})^\gamma \log(\hat{\mathbf{y}}_{ijk}), \quad (9)$$

where K is the number of semantic classes, $\hat{\mathbf{y}}_{ijk}$ is the predicted probability for class k at pixel (i, j) , and γ is the focusing parameter (typically set to 2). The cross-entropy loss \mathcal{L}_{CE} aims to align the predicted and true probability distributions, while the focal loss $\mathcal{L}_{\text{Focal}}$ down-weights easy examples, emphasizing hard-to-classify pixels to improve segmentation performance on underrepresented classes.

IV. EXPERIMENTS

A. Experimental Details

Datasets. We evaluate our spike-driven framework on a public available dataset for fair comparison with baselines and a private in-house dataset to illustrate the effectiveness of real-world application. Details are provided as follows:

1) *EndoVis18 Dataset.* The 2018 MICCAI EndoVis Scene Segmentation Challenge (EndoVis18) dataset [53] features more complex surgical scenes and has been widely adopted in prior studies [6], [7]. It comprises 15 videos, each containing

149 frames of resolution 1024×1280 . Following the standard protocol in [54], we use sequences 2, 5, 9, and 15 for testing, while the remaining sequences are used for training. The instrument categories evaluated include Bipolar Forceps (BF), Prograsp Forceps (PF), Large Needle Driver (LND), Suction Instrument (SI), Clip Applier (CA), Monopolar Curved Scissors (MCS), and Ultrasound Probe (UP).

2) *In-House SurgBleed Dataset*. We curated an in-house dataset of hepatobiliary surgical videos, named the Surgical Bleeding Tracking (SurgBleed) dataset, to facilitate bleeding area segmentation and surgical alert applications. The dataset comprises 70 videos collected from 25 surgical cases, recorded at 30 frames per second with a resolution of 720×1280 pixels and an overall duration of 4,721.6 seconds. Expert surgeons manually annotated the bleeding regions using polygonal masks every 10 frames, resulting in 6,703 labeled frames. Frames without bleeding were excluded from the annotated clips. On average, the annotated bleeding regions occupy 35,012.86 pixels per frame, corresponding to roughly a 187×187 pixel area or 3.79% of the full frame. As representative examples illustrated in Supplementary B, the main challenges arise from the irregular and highly dynamic bleeding boundaries, *i.e.*, large variations in bleeding size and frequent occlusions from surgical instruments. *This in-house dataset is designed to better reflect real-world surgical environments*, where accurate and timely small bleeding area segmentation is far more critical than instrument recognition, as it directly impacts surgical decision-making and patient safety. In the experiment, a patient-level data split is applied, with approximately 80% of the cases used for training and the remaining 20% for testing. This yields 4,753 qualified 4-frame clips for training and 910 clips for testing.

Implementation Details. Our model is partially implemented using SpikingJelly [55]. We employ a parametric LIF neuron with a soft reset, where backpropagation through the reset path is preserved. In the segmentation head, the SpikeFPN module utilizes an IntIF neuron with $Z = 4$. During training, we apply several data augmentation strategies, including random resizing within the range of 0.3–0.7, cropping to an input size of 512×640 for the EndoVis18 dataset and 384×640 for the SurgBleed dataset, random horizontal flipping, and photometric distortion. Each input video clip contains 4 frames (*i.e.*, $T = 4$), consistent with prior works on video semantic segmentation [20], [21], [54].

For surgical-scene MAE pretraining, *we utilize the entire training set without introducing additional unlabeled data*. This setup ensures a fair comparison with models trained directly on the surgical video segmentation task, as our primary goal is to demonstrate the effectiveness of video-masked pretraining within the SNN-based framework. During pretraining, 50% (α) of the input pixel tubes are randomly masked. The model is trained on 4 or 8 NVIDIA A6000 GPUs with a batch size of 16 and a learning rate of 4×10^{-4} for the 16M and 56.3M spike-driven encoder variants, respectively. The decoder adopts an 8-layer ViT [28] that applies space-time self-attention to reconstruct the video clips. Pretraining is conducted for 200 epochs using a cosine annealing schedule with a maximum of 250 epochs.

For surgical video segmentation finetuning, the memory read and fusion module outputs 128 or 256 channels, which are subsequently processed by the SpikeFPN with matching channel dimensions for the 16M and 56.3M encoder variants, respectively. The final layer produces per-pixel class probabilities, *i.e.*, 8 classes for the EndoVis18 dataset and 2 classes for the SurgBleed dataset. Training on both datasets is conducted with a batch size of 16 and a learning rate of 4×10^{-4} , using 4 or 8 NVIDIA A6000 GPUs for the two model variants. The models are finetuned for 80 epochs under a cosine annealing schedule with a maximum of 120 epochs.

Evaluation Metrics. We evaluate the segmentation performance using the Intersection over Union (**IoU**), which quantifies the overlap between predicted and ground-truth regions as the ratio of their intersection to their union. For the EndoVis18 dataset, both class-wise IoU and mean IoU (**mIoU**) are reported to provide a comprehensive assessment. To evaluate the efficiency of SNNs, we report power consumption (**Power**) in milli-joules (mJ), estimated based on the number of AC or MAC floating-point operations required by each model. Inference time (**Latency**) in milli-seconds (ms) is also reported to assess runtime performance, estimated on the AMD Xilinx ZCU104 platform [47] as is described in Sec. III-A. This setup excludes GPU support, ensuring a fair evaluation of computational efficiency for real-world applications.

B. Comparison on EndoVis18 Dataset

Baselines. Our SpikeSurgSeg is a task-specific model. Accordingly, we compare it with several task-specific ANN-based baselines, including ISINet [54], S3Net [58], and MATIS [59]. In contrast, recent methods have mostly shifted toward prompt-based paradigms that adapt SAM or SAM2 for downstream tasks and rely on user-provided prompts as auxiliary inputs. We therefore include TrackAnything [56], PerSAM [57], SurgicalSAM [6], and SurgicalSAM2 [7] as additional baselines. Since prompts convey explicit prior knowledge about target objects, these models generally yield higher accuracy. For a fair comparison, we adopt the simplest configuration, *i.e.*, a single-point prompt, for all prompt-based baselines.

Results. As shown in Table I, SpikeSurgSeg delivers a markedly more balanced trade-off between accuracy, latency, and energy efficiency compared with both prompt-based and task-specific ANN baselines. While prompt-driven SAM variants achieve relatively strong category-level IoU on certain instruments, largely due to the injected prior via point prompts, their performance remains inconsistent across categories, and this advantage comes at the cost of substantially higher computational overhead (*e.g.*, ~ 500 – 560 mJ power and > 160 ms latency for SAM-based methods). Although SurgicalSAM2 achieves moderate accuracy (37.69% mIoU) under reduced computation, its performance degrades sharply on several key instrument categories (*e.g.*, LND and UP), indicating that simply scaling down foundation-model architectures cannot reliably meet the fine-grained segmentation requirements of surgical scenes. This is further validated in Fig. 4. Task-specific ANN models such as ISINet, S3Net, and MATIS attain competitive mIoU values (40–49%), yet they exhibit similarly

TABLE I: Surgical Video Segmentation on EndoVis18 Dataset. Our spike-driven models achieve comparable mIoU with most ANN-based models while significantly reducing inference time and power consumption. For fairness, all prompt-based baselines use a single-point prompt as additional input. Note that TrackAnything [56], PerSAM [57] and SurgicalSAM [6] uses SAM-B as the base model, whereas SurgicalSAM2 [7] adopts the most lightweight SAM2-Small as its base model.

| Models | Methods | SNNs | Param | Power (mJ) | Latency (ms) | cIoU | mIoU | Instrument Category IoU | | | | | | |
|----------------------|---------------------|------|--------|------------|--------------|-------|-------|-------------------------|-------|-------|-------|-------|-------|-------|
| | | | | | | | | BF | PF | LND | SI | CA | MCS | UP |
| Prompt-Based Models | TrackAnything [56] | ✗ | 91.0M | 533.3 | 167.7 | 40.36 | 20.62 | 30.20 | 12.87 | 24.46 | 9.17 | 0.19 | 55.03 | 12.41 |
| | PerSAM [57] | ✗ | 91.0M | 533.3 | 167.7 | 49.21 | 34.55 | 51.26 | 34.40 | 46.75 | 16.45 | 15.07 | 52.28 | 25.62 |
| | SurgicalSAM [6] | ✗ | 93.5M | 560.6 | 176.3 | 74.12 | 43.67 | 80.32 | 50.78 | 19.73 | 43.81 | 5.23 | 88.56 | 17.32 |
| | SurgicalSAM2 [7] | ✗ | 49.3M | 208.4 | 65.6 | 70.60 | 37.69 | 77.23 | 52.63 | 0.12 | 42.78 | 0.00 | 91.07 | 0.00 |
| Task-Specific Models | ISINet [54] | ✗ | 162.5M | 1527.2 | 480.3 | 73.03 | 40.21 | 73.83 | 48.61 | 30.98 | 37.68 | 0.00 | 88.16 | 2.16 |
| | S3Net [58] | ✗ | 71.4M | 524.4 | 164.9 | 75.81 | 42.58 | 77.22 | 50.87 | 19.83 | 50.59 | 0.00 | 92.12 | 7.44 |
| | MATIS-Frame [59] | ✗ | 97.0M | 588.8 | 185.2 | 82.37 | 48.65 | 83.35 | 38.82 | 40.19 | 64.49 | 4.32 | 93.18 | 16.17 |
| | SpikeSurgSeg (Ours) | ✓ | 21.1M | 40.8 | 8.2 | 74.12 | 41.65 | 81.84 | 46.98 | 40.27 | 29.78 | 1.74 | 90.93 | 0.0 |

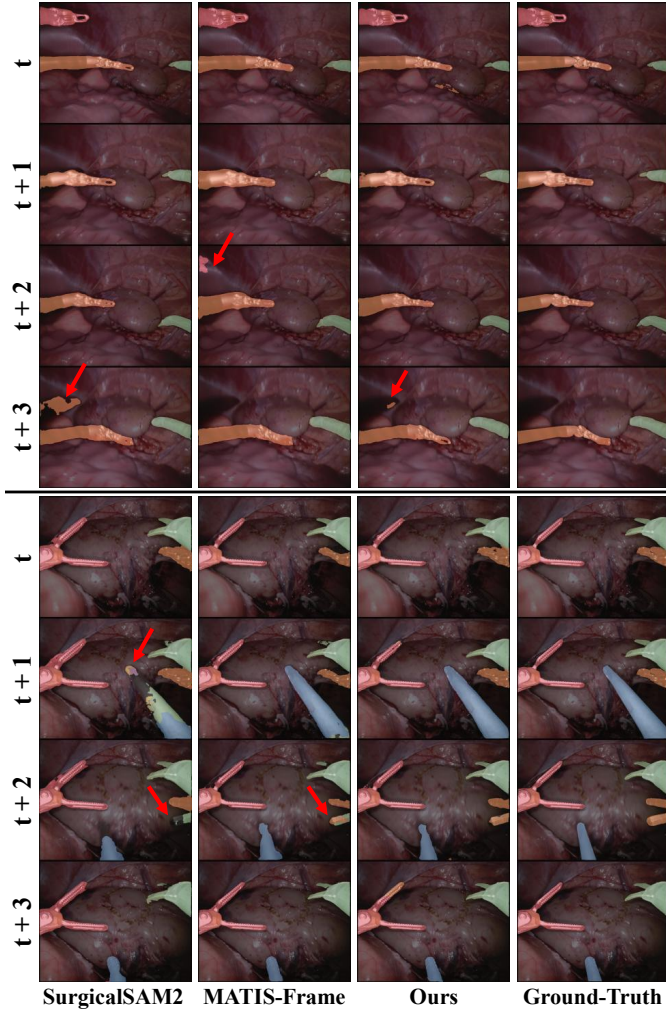


Fig. 4: Qualitative Results on EndoVis18 Dataset. Our SNN-based model maintains high efficiency while reducing false positives and inference time, benefiting from the inherent sparsity of spike-driven computation.

high power consumption (524–1527 mJ) and inference latency (165–480 ms), making real-time deployment in the operating room impractical. In contrast, the small SpikeSurgSeg vari-

ant achieves comparable mIoU (41.65%) with only 21.1M parameters while reducing power consumption by 13–37× and latency by 20–58× relative to ANN counterparts. The larger variant further improves accuracy (43.21% mIoU) and category IoUs while still operating under 180 mJ power and 36 ms latency, well within real-time constraints in non-GPU setting. These results collectively demonstrate that spike-driven architectures can match the segmentation quality of contemporary models while drastically reducing computational cost, offering a more practical path toward deployable intra-operative intelligence.

C. Comparison on SurgBleed Dataset

Baselines. For prompt-based models, we evaluate two types of SAM-based results. The first is zero-shot inference, in which SAM-Base [40] and SAM2-Base+ [21] are directly tested on the SurgBleed dataset using a single-point prompt derived from the ground-truth bleeding mask. The second is finetuned performance, where SAM2-Base+ is trained on the SurgBleed dataset for 100 epochs with a learning rate of 5×10^{-5} following SurgicalSAM2 [7]. Additionally, we also include finetuning with the adapter proposed in [60]. For task-specific models, ISINet [54] and MATIS [59] are re-trained on the SurgBleed dataset.

Results. As shown in Tab. II, our 21.1M SpikeSurgSeg model attains slightly lower mIoU than the SOTA task-specific model MATIS on surgical bleeding segmentation, yet delivers substantial efficiency advantages, reducing power consumption and latency by 14.4× and 22.7×, respectively. In the zero-shot setting, SAM trails SAM2 by 3.7% mIoU, highlighting the necessity of video-based architectures for surgical video understanding. When finetuned with the SAM2-based pipeline, our SNN model still achieves competitive accuracy while providing over 9.6× lower power consumption and 15.1× faster inference compared with SAM2-Base+ that replies on an extra single-point user prompt as input. Qualitative examples in Fig. 5 further demonstrate that our SNN approach produces accurate and stable segmentation results. Collectively, these findings underscore the real-time potential of our spike-driven

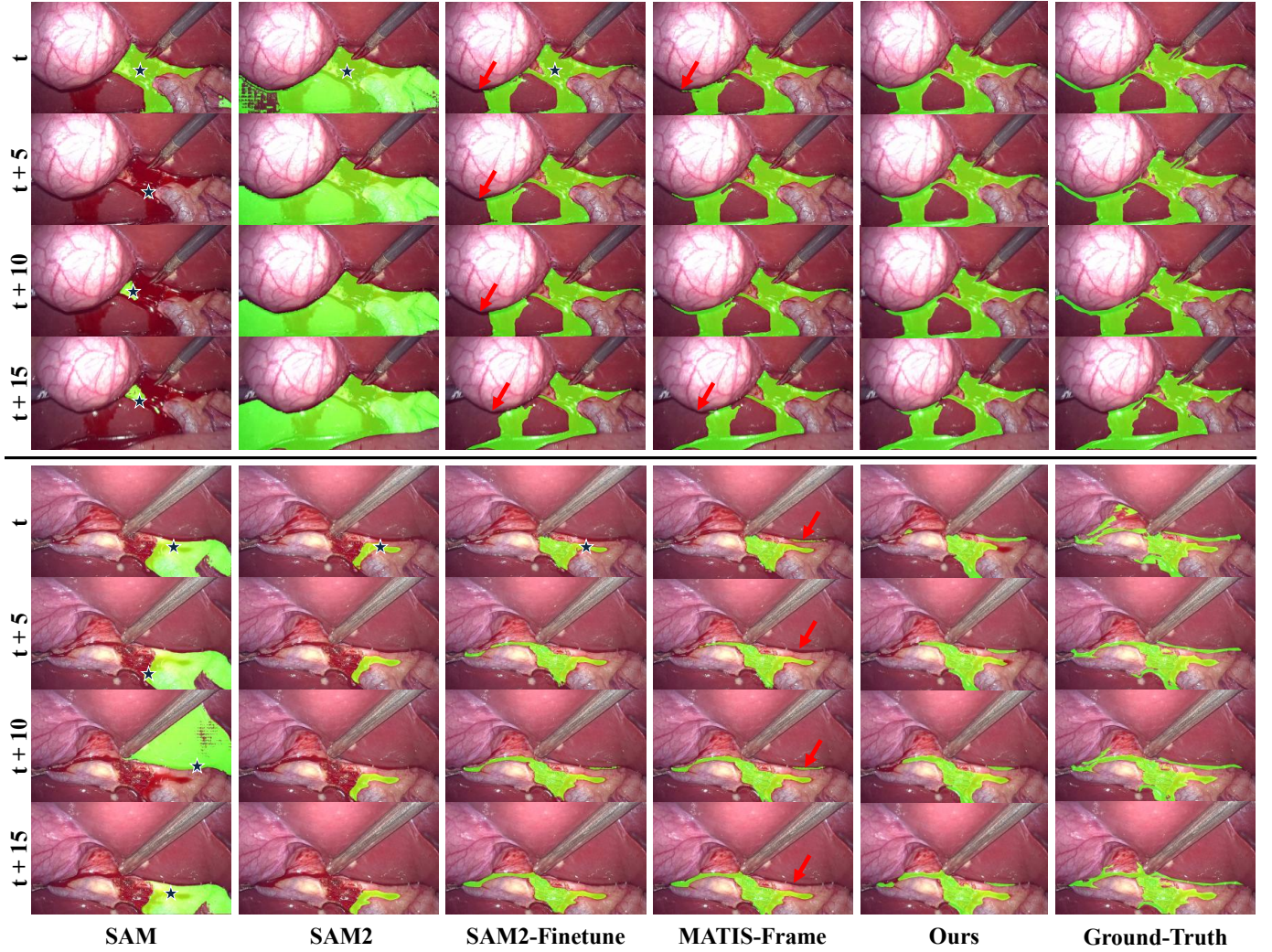


Fig. 5: **Qualitative Results on SurgBleed Dataset.** Compared with the task-specific MATIS-Frame method and the prompt-based SAM2-Finetune method, our SNN-based model achieves comparable or even superior bleeding segmentation performance, while maintaining substantially lower energy consumption and inference latency.

TABLE II: **Surgical Bleeding Segmentation on SurgBleed Dataset.** We use SAM-Base model for the SAM baseline and SAM2-Base+ for all SAM2 baselines.

| Models | Methods | SNNs | Param | Power (mJ) | Latency (ms) | mIoU |
|----------------------|---------------------|------|--------|-------------|--------------|--------------|
| Prompt-Based Models | SAM [40] | ✗ | 91.0M | 400.0 | 125.8 | 28.40 |
| | SAM2 [21] | ✗ | 80.8M | 293.3 | 92.2 | 32.10 |
| | SAM2-Finetune [7] | ✗ | 80.8M | 293.3 | 92.2 | 69.79 |
| | SAM2-Adapter [60] | ✗ | 81.3M | 308.1 | 96.9 | 69.40 |
| Task-Specific Models | ISINet [54] | ✗ | 162.5M | 1145.4 | 360.2 | 64.95 |
| | MATIS-Frame [59] | ✗ | 97.0M | 441.6 | 138.9 | 70.80 |
| | SpikeSurgSeg (Ours) | ✓ | 21.1M | 30.6 | 6.1 | 69.60 |
| | | ✓ | 62.1M | 134.1 | 26.9 | 72.50 |

framework, whose feed-forward computation consists solely of efficient addition operations.

D. Ablation Study

1) *Pretraining Stage:* To better understand what drives effective representation learning in our spike-based pretraining framework, we perform a series of ablations. We analyze how

pretraining data scale, unlabeled video augmentation, mask ratio, and KD loss each contribute to downstream segmentation accuracy as follows.

- **Part of Pretraining Data.** To assess how pretraining dataset size influences representation quality, we pretrain the model using only a part of the training data. As shown in Fig. 6 (a) and (b), expanding the pretraining set consistently improves downstream segmentation performance on both EndoVis18 and SurgBleed under mask ratios of 0.5 and 0.7, respectively. The gains become particularly pronounced when the pretraining data portion approaches the full dataset, suggesting that larger-scale video exposure is crucial for learning robust spatiotemporal representations. Qualitative comparisons in Fig. 7 further confirm this trend: insufficient pretraining data often leads to fragmented boundaries and temporally unstable predictions.
- **Extra Unlabeled Pretraining Data.** We further investigate the value of leveraging extra unlabeled data during pretraining. Specifically, for EndoVis18 instrument seg-

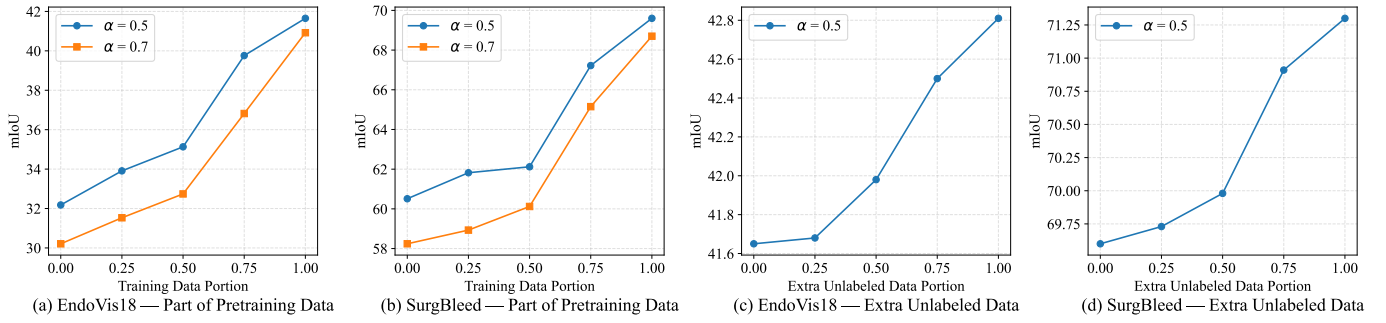


Fig. 6: **Pretraining Data Size vs Downstream Surgical Segmentation Performance.** (a-b) Using only part of the training data for masked video pretraining shows that increasing the pretraining set size consistently boosts downstream mIoU on both EndoVis18 and SurgBleed. (c-d) Incorporating additional unlabeled data further improves performance in a monotonic manner, highlighting the benefit of large-scale unlabeled surgical video data for strengthening spatiotemporal representation learning.

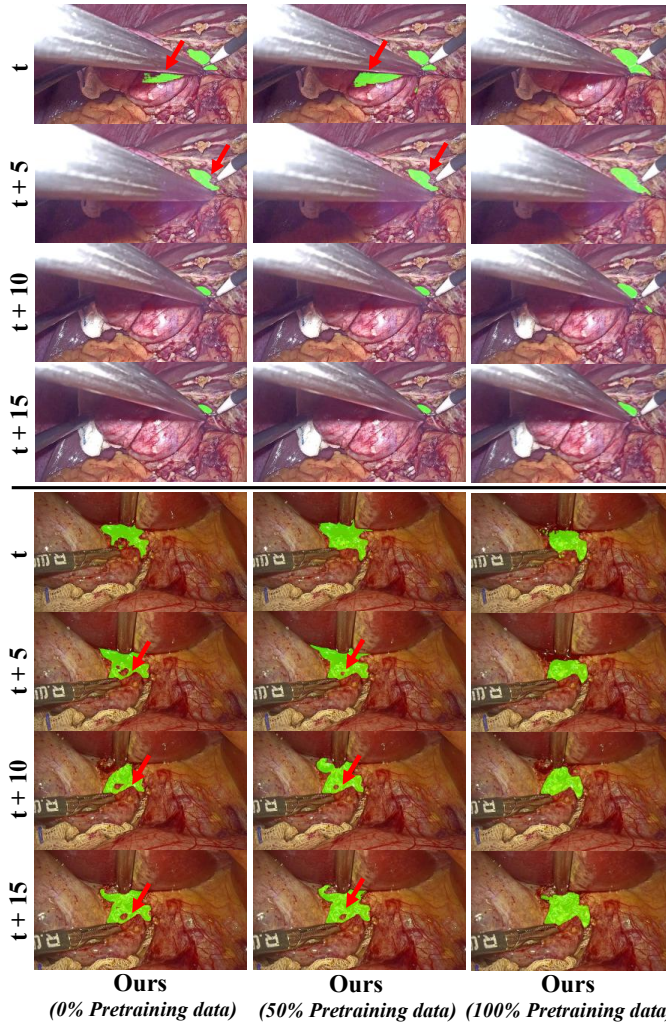


Fig. 7: **Qualitative Comparison of Models with and without VideoMAE Pretraining.** Using 0% or only 50% of the data for pretraining results in fragmented and temporally inconsistent predictions, whereas pretraining on the full dataset (100%) produces more accurate and coherent segmentation results.

mentation, we incorporate extra unlabeled videos from EndoVis17 [53], and for SurgBleed, we add the unlabeled frames from the original surgical video data. We denote the amount of added data using a portion ranging from

TABLE III: **Ablation on the KD Loss During Pretraining.**

| Use KD Loss | EndoVis18 | | SurgBleed | |
|----------------|---------------|--------|---------------|--------|
| | Pixel Error ↓ | mIoU ↑ | Pixel Error ↓ | mIoU ↑ |
| ✓ | 7.53 | 69.60 | 6.76 | 41.65 |
| ✗ | 8.22 | 69.14 | 7.98 | 41.19 |

0 to 1 relative to the original pretraining dataset size. As shown in Fig. 6 (c) and (d), increasing the quantity of unlabeled pretraining data yields consistent performance gains on both datasets. These results emphasize the strong potential of large-scale unlabeled surgical video data to enhance downstream surgical scene understanding.

- **Mask Ratio.** The ablations of mask ratio on downstream surgical segmentation performance for both datasets are presented in Fig. 8. The results indicate that mask ratios of 0.5 or 0.6 yield the best representation learning capability for our SNN-based framework. Unlike prior ANN-based models [50], which can tolerate high masking rates above 0.8, SNNs rely on sparse spiking features, making them more sensitive to excessive information removal. Consequently, a moderate mask ratio is necessary to preserve sufficient spatiotemporal cues for effective representation learning.
- **KD Loss.** We evaluate the role of KD loss in improving both reconstruction fidelity (Pixel Error) during pretraining and downstream segmentation performance (mIoU) after finetuning. As reported in Tab. III, removing KD loss consistently increases Pixel Error on EndoVis18 (7.53 to 8.22) and SurgBleeding (6.76 to 7.98), reflecting weaker feature alignment in the pretraining stage. This reduction in reconstruction quality is accompanied by small yet steady declines in downstream mIoU on both datasets, confirming the regularizing effect of KD loss.

2) *Finetuning Stage:* We analyze how the pretrained SNN encoder behaves when adapted to downstream surgical tasks. We assess both its generalization ability to recognition problems and the impact of freezing versus updating the backbone during segmentation.

- **Generalization to Other Downstream Task.** To assess how well the pretrained SNN encoder transfers beyond segmentation, we finetune it for two recognition tasks:

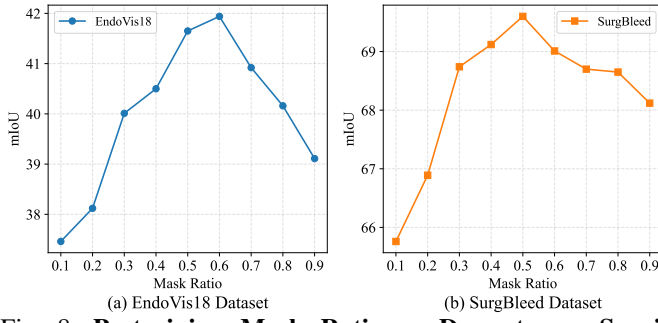


Fig. 8: **Pretraining Mask Ratio vs Downstream Surgical Segmentation Performance.** Moderate masking levels (0.5–0.6) produce the best representations for our SNN-based framework, whereas overly high ratios degrade performance due to the sparse nature of spiking features.

TABLE IV: **Pretraining Generalization to Downstream Recognition Task.** We evaluate how pretraining benefits recognition by comparing a SNN backbone with and without pretraining when finetuned for 7-instrument classification on EndoVis18 and bleeding recognition on SurgBleed.

| Use Pretraining | Instrument (EndoVis18) | Bleeding (SurgBleed) |
|-----------------|------------------------|----------------------|
| | Accuracy \uparrow | Accuracy \uparrow |
| \times | 81.2 | 91.3 |
| \checkmark | 73.5 | 85.8 |

TABLE V: **Ablation on SNN Backbone Freezing or Fully Training During Downstream Task Finetunning.**

| Backbone Freezing | EndoVis18 | SurgBleed |
|-------------------|-----------------|-----------------|
| | mIoU \uparrow | mIoU \uparrow |
| \times | 40.89 | 68.71 |
| \checkmark | 41.65 | 69.60 |

7-instrument classification on EndoVis18 and bleeding detection on the extended SurgBleed dataset (balanced 1:1 for bleeding vs. non-bleeding). A spiking linear head is attached to the encoder output, and performance is measured by (mean) accuracy. As shown in Tab. IV, pretraining yields clear gains on both tasks, improving instrument recognition from 73.5 to 81.2 and bleeding detection from 85.8 to 91.3. These consistent improvements demonstrate that the pretrained representations capture transferable spatiotemporal cues beneficial across diverse surgical video understanding tasks.

- **SNN Backbone Freezing.** We further investigate whether the pretrained SNN backbone should be frozen or fully finetuned during downstream segmentation. As shown in Tab. V, allowing the backbone to update brings slight mIoU improvements on EndoVis18 and SurgBleed. Notably, the frozen backbone already delivers performance close to the fully finetuned variant. This observation suggests that pretraining has endowed the model with a stable, high-quality representation of surgical scenes, making extensive parameter updates unnecessary for effective downstream segmentation.

E. Discussion

Computational Redundancy. While generic foundation models such as SAM and SAM2 show strong generalization across natural visual domains, our experiments reveal that their large-scale architectures introduce considerable computational redundancy in task-specific surgical video analysis. As shown in Tab. I and II, these models, though versatile, struggle to satisfy the strict real-time and energy constraints of intra-operative environments. In contrast, SpikeSurgSeg achieves comparable segmentation accuracy with drastically lower power consumption and latency through its domain-adaptive neuromorphic design. This finding challenges the necessity of deploying monolithic foundation models in surgical systems, suggesting that neuromorphic architectures may offer a more practical route toward clinically deployable intelligent surgery. Nevertheless, it remains an open question how to design a foundation model that balances the accuracy and generalization of large-scale vision models with the efficiency and sparsity of brain-like computation.

Feasibility of Deployment. Previous work [45] has demonstrated the feasibility of deploying SNN-based models on neuromorphic hardware, achieving even lower latency and energy consumption than theoretical estimates. Given that our architecture shares fundamental similarities with the model presented in [45], the deployment of our SNN-based framework on neuromorphic hardware is expected to be equally feasible. Nevertheless, as highlighted in a recent *Nature* review [10] together with analysis in [61], the neuromorphic hardware ecosystem remains in an early developmental stage, particularly in supporting large-scale spike-driven model training and optimization. Such asymmetry is typical in emerging computing paradigms, where algorithmic advances often precede the maturation of corresponding hardware platforms. Overall, these trends indicate a promising yet still emerging pathway toward neuromorphic deployment of our model.

V. CONCLUSION

We presented SpikeSurgSeg, a spike-driven video Transformer that unifies SNNs with self-supervised representation learning for real-time surgical scene segmentation. Experimental results on EndoVis18 and SurgBleed demonstrate that our model attains comparable accuracy to SOTA ANN counterparts while reducing energy consumption and inference latency by more than an order of magnitude. In particular, the biologically inspired spiking dynamics align naturally with the temporal continuity of surgical videos, enabling efficient spatiotemporal modeling without reliance on GPUs. Moreover, the integration of masked autoencoding pretraining and semantic knowledge distillation allows the model to internalize both structural and semantic priors, effectively narrowing the gap between spike-driven and conventional visual representations. The overall framework establishes a balanced trade-off between accuracy, latency, and energy efficiency. Future work will extend this paradigm toward larger-scale pretraining on unlabeled surgical videos and multimodal spike-driven perception, advancing the development of real-time, deployable, and sustainable intelligent surgical systems.

REFERENCES

[1] G. Qin, H. Liu, X. Zhang, W. Li, Y. Guo, and C. Guo, "Semi-supervised medical hyperspectral image segmentation using adversarial consistency constraint learning and cross indication network," *IEEE TIP*, 2025.

[2] C. G. A. Viviers, L. Filatova, M. Termeer, P. H. N. de With, and F. van der Sommen, "Advancing 6-dof instrument pose estimation in variable x-ray imaging geometries," *IEEE TIP*, 2024.

[3] Y. Long, A. Lin, D. H. C. Kwok, L. Zhang, Z. Yang, K. Shi, L. Song, J. Fu, H. Lin, W. Wei, K. Chen, X. Chu, Y. Hu, H. C. Yip, P. W. Y. Chiu, P. Kazanzides, R. H. Taylor, Y. Liu, Z. Chen, Z. Wang, null, and Q. Dou, "Surgical embodied intelligence for generalized task autonomy in laparoscopic robot-assisted surgery," *Science Robotics*, 2025.

[4] D. Kiyasseh, R. Ma, T. F. Haque, B. J. Miles, C. Wagner, D. Donoho, A. Anandkumar, and A. J. Hung, "A vision transformer for decoding surgeon activity from surgical videos," *Nature Biomedical Engineering*, 2023.

[5] Y. Jin, Y. Yu, C. Chen, Z. Zhao, P.-A. Heng, and D. Stoyanov, "Exploring intra-and inter-video relation for surgical semantic scene segmentation," *IEEE TMI*, 2022.

[6] W. Yue, J. Zhang, K. Hu, Y. Xia, J. Luo, and Z. Wang, "Surgicalsam: Efficient class prompttable surgical instrument segmentation," in *AAAI*, 2024.

[7] H. Liu, E. Zhang, J. Wu, M. Hong, and Y. Jin, "Surgical sam 2: Real-time segment anything in surgical video by efficient frame pruning," *NeurIPS Workshop*, 2024.

[8] L. Maier-Hein, M. Eisenmann, D. Sarikaya, K. März, T. Collins, A. Malpani, J. Fallert, H. Feussner, S. Giannarou, P. Mascagni *et al.*, "Surgical data science—from concepts toward clinical translation," *MIA*, 2022.

[9] M. Carstens, F. M. Rinner, S. Bodenstedt, A. C. Jenke, J. Weitz, M. Distler, S. Speidel, and F. R. Kolbinger, "The dresden surgical anatomy dataset for abdominal organ segmentation in surgical data science," *Nature Scientific Data*, 2023.

[10] D. Kudithipudi, C. Schuman, C. M. Vineyard, T. Pandit, C. Merkel, R. Kubendran, J. B. Aimone, G. Orchard, C. Mayr, and R. Benosman, "Neuromorphic computing at scale," *Nature*, 2025.

[11] G. Li, L. Deng, H. Tang, G. Pan, Y. Tian, K. Roy, and W. Maass, "Brain-inspired computing: A systematic survey and future trends," *Proceedings of the IEEE*, 2024.

[12] W. Fang, Z. Yu, Y. Chen, T. Huang, T. Masquelier, and Y. Tian, "Deep residual learning in spiking neural networks," *NeurIPS*, 2021.

[13] M. Yao, G. Zhao, H. Zhang, Y. Hu, L. Deng, Y. Tian, B. Xu, and G. Li, "Attention spiking neural networks," *IEEE TPAMI*, 2023.

[14] M. Yao, J. Hu, T. Hu, Y. Xu, Z. Zhou, Y. Tian, B. Xu, and G. Li, "Spike-driven transformer v2: Meta spiking neural network architecture inspiring the design of next-generation neuromorphic chips," *ICLR*, 2024.

[15] Q. Su, Y. Chou, Y. Hu, J. Li, S. Mei, Z. Zhang, and G. Li, "Deep directly-trained spiking neural networks for object detection," in *ICCV*, 2023.

[16] X. Luo, M. Yao, Y. Chou, B. Xu, and G. Li, "Integer-valued training and spike-driven inference spiking neural network for high-performance and energy-efficient object detection," *ECCV*, 2024.

[17] Q. Su, W. He, X. Wei, B. Xu, and G. Li, "Multi-scale full spike pattern for semantic segmentation," *Neural Networks*, 2024.

[18] H. Wang, X. Liang, T. Zhang, Y. Gu, and W. Geng, "Pssd-transformer: Powerful sparse spike-driven transformer for image semantic segmentation," in *ACM MM*, 2024.

[19] Z. Lei, M. Yao, J. Hu, X. Luo, Y. Lu, B. Xu, and G. Li, "Spike2former: Efficient spiking transformer for high-performance image segmentation," in *AAAI*, 2025.

[20] S. Zou, Q. Li, W. Ji, J. Li, Y. Yang, G. Li, and C. Dong, "Spiky-ideoformer: An efficient spike-driven video transformer with hamming attention and o(t) complexity," in *ICML*, 2025.

[21] N. Ravi, V. Gabeur, Y.-T. Hu, R. Hu, C. Ryali, T. Ma, H. Khedr, R. Rädle, C. Rolland, L. Gustafson, E. Mintun, J. Pan, K. V. Alwala, N. Carion, C.-Y. Wu, R. Girshick, P. Dollár, and C. Feichtenhofer, "Sam 2: Segment anything in images and videos," *arXiv preprint arXiv:2408.00714*, 2024.

[22] S. Deng and S. Gu, "Optimal conversion of conventional artificial neural networks to spiking neural networks," in *ICLR*, 2021.

[23] Y. Li, Y. Guo, S. Zhang, S. Deng, Y. Hai, and S. Gu, "Differentiable spike: Rethinking gradient-descent for training spiking neural networks," *NeurIPS*, 2021.

[24] C. Zhou, H. Zhang, L. Yu, Y. Ye, Z. Zhou, L. Huang, Z. Ma, X. Fan, H. Zhou, and Y. Tian, "Direct training high-performance deep spiking neural networks: a review of theories and methods," *Frontiers in Neuroscience*, 2024.

[25] Y. Hu, L. Deng, Y. Wu, M. Yao, and G. Li, "Advancing spiking neural networks toward deep residual learning," *IEEE TNNLS*, 2024.

[26] Z. Zhou, Y. Zhu, C. He, Y. Wang, S. Yan, Y. Tian, and L. Yuan, "Spikformer: When spiking neural network meets transformer," in *ICLR*, 2022.

[27] M. Yao, J. Hu, Z. Zhou, L. Yuan, Y. Tian, B. Xu, and G. Li, "Spike-driven transformer," *NeurIPS*, 2024.

[28] A. Dosovitskiy, L. Beyer, A. Kolesnikov, D. Weissenborn, X. Zhai, T. Unterthiner, M. Dehghani, M. Minderer, G. Heigold, S. Gelly *et al.*, "An image is worth 16x16 words: Transformers for image recognition at scale," in *ICLR*, 2020.

[29] M. Yao, X. Qiu, T. Hu, J. Hu, Y. Chou, K. Tian, J. Liao, L. Leng, B. Xu, and G. Li, "Scaling spike-driven transformer with efficient spike firing approximation training," *IEEE TPAMI*, 2025.

[30] A. Vaswani, N. Shazeer, N. Parmar, J. Uszkoreit, L. Jones, A. N. Gomez, Ł. Kaiser, and I. Polosukhin, "Attention is all you need," *NeurIPS*, 2017.

[31] K. He, X. Chen, S. Xie, Y. Li, P. Dollár, and R. Girshick, "Masked autoencoders are scalable vision learners," in *CVPR*, 2022.

[32] Z. Tong, Y. Song, J. Wang, and L. Wang, "Videomae: Masked autoencoders are data-efficient learners for self-supervised video pre-training," *NeurIPS*, 2022.

[33] C. Wei, H. Fan, S. Xie, C.-Y. Wu, A. Yuille, and C. Feichtenhofer, "Masked feature prediction for self-supervised visual pre-training," in *CVPR*, 2022.

[34] P. Gao, T. Ma, H. Li, Z. Lin, J. Dai, and Y. Qiao, "Mcmae: Masked convolution meets masked autoencoders," *NeurIPS*, 2022.

[35] K. Tian, Y. Jiang, Q. Diao, C. Lin, L. Wang, and Z. Yuan, "Designing bert for convolutional networks: Sparse and hierarchical masked modeling," *ICLR*, 2023.

[36] Y. Chen, Y. Liu, D. Jiang, X. Zhang, D. Wenrui, H. Xiong, and Q. Tian, "Sdae: Self-distilled masked autoencoder," in *ECCV*, 2022.

[37] M. Oquab, T. Darcret, T. Moutakanni, H. Vo, M. Szafraniec, V. Khalidov, P. Fernandez, D. Haziza, F. Massa, A. El-Nouby *et al.*, "Dinov2: Learning robust visual features without supervision," *TMLR*, 2024.

[38] N. A. Shah, W. G. C. Bandara, S. Skider, S. S. Vedula, and V. M. Patel, "Csmae: Cataract surgical masked autoencoder (mae) based pre-training," in *IEEE ISBI*, 2025.

[39] Z. Z. Zhao, Y. Jin, G. Xiaojie, Q. Dou, and P.-A. Heng, "Learning motion flows for semi-supervised instrument segmentation from robotic surgical video," in *MICCAI*, 2020.

[40] A. Kirillov, E. Mintun, N. Ravi, H. Mao, C. Rolland, L. Gustafson, T. Xiao, S. Whitehead, A. C. Berg, W.-Y. Lo *et al.*, "Segment anything," in *ICCV*, 2023.

[41] J. Ma, Y. He, F. Li, L. Han, C. You, and B. Wang, "Segment anything in medical images," *Nature Communications*, 2024.

[42] Z. Zhou, O. Alabi, M. Wei, T. Vercauteren, and M. Shi, "Text promptable surgical instrument segmentation with vision-language models," *NeurIPS*, 2023.

[43] J. N. Paranjape, N. G. Nair, S. Sikder, S. S. Vedula, and V. M. Patel, "Adaptivesam: Towards efficient tuning of sam for surgical scene segmentation," in *Annual Conference on Medical Image Understanding and Analysis*, 2024.

[44] J. Wu, Z. Wang, M. Hong, W. Ji, H. Fu, Y. Xu, M. Xu, and Y. Jin, "Medical sam adapter: Adapting segment anything model for medical image segmentation," *MIA*, 2025.

[45] M. Yao, O. Richter, G. Zhao, N. Qiao, Y. Xing, D. Wang, T. Hu, W. Fang, T. Demirci, and M. D. Marchi, "Spike-based dynamic computing with asynchronous sensing-computing neuromorphic chip," *Nature Communications*, 2025.

[46] M. Horowitz, "1.1 computing's energy problem (and what we can do about it)," in *ISSCC*, 2014.

[47] J. Li, G. Shen, D. Zhao, Q. Zhang, and Y. Zeng, "Firefly: A high-throughput hardware accelerator for spiking neural networks with efficient dsp and memory optimization," *IEEE TVLSI*, 2023.

[48] S. Zou, Y. Mu, W. Ji, Z.-A. Wang, X. Zuo, S. Wang, W. Si, and L. Cheng, "Highly efficient 3d human pose tracking from events with spiking spatiotemporal transformer," *IEEE TCSV*, 2025.

[49] W. Yu, M. Luo, P. Zhou, C. Si, Y. Zhou, X. Wang, J. Feng, and S. Yan, "Metaformer is actually what you need for vision," in *CVPR*, 2022.

[50] L. Wang, B. Huang, Z. Zhao, Z. Tong, Y. He, Y. Wang, Y. Wang, and Y. Qiao, "Videomae v2: Scaling video masked autoencoders with dual masking," in *CVPR*, 2023.

- [51] M. Paul, M. Danelljan, L. Van Gool, and R. Timofte, “Local memory attention for fast video semantic segmentation,” in *IROS*, 2021.
- [52] H. Zhao, J. Shi, X. Qi, X. Wang, and J. Jia, “Pyramid scene parsing network,” in *CVPR*, 2017.
- [53] M. Allan, S. Kondo, S. Bodenstedt, S. Leger, R. Kadkhodamohammadi, I. Luengo, F. Fuentes, E. Flouty, A. Mohammed, M. Pedersen *et al.*, “2018 robotic scene segmentation challenge,” *arXiv preprint arXiv:2001.11190*, 2020.
- [54] C. González, L. Bravo-Sánchez, and P. Arbelaez, “Isinet: an instance-based approach for surgical instrument segmentation,” in *MICCAI*, 2020.
- [55] W. Fang, Y. Chen, J. Ding, D. Chen, Z. Yu, H. Zhou, Y. Tian, and other contributors, “Spikingjelly,” <https://github.com/fangwei123456/spikingjelly>, 2020, accessed: 2025-12-01.
- [56] J. Yang, M. Gao, Z. Li, S. Gao, F. Wang, and F. Zheng, “Track anything: Segment anything meets videos,” *arXiv preprint arXiv:2304.11968*, 2023.
- [57] R. Zhang, Z. Jiang, Z. Guo, S. Yan, J. Pan, H. Dong, P. Gao, and H. Li, “Personalize segment anything model with one shot,” *arXiv preprint arXiv:2305.03048*, 2023.
- [58] B. Baby, D. Thapar, M. Chasmai, T. Banerjee, K. Dargan, A. Suri, S. Banerjee, and C. Arora, “From forks to forceps: A new framework for instance segmentation of surgical instruments,” in *WACV*, 2023.
- [59] N. Ayobi, A. Pérez-Rondón, S. Rodríguez, and P. Arbeláez, “Matis: Masked-attention transformers for surgical instrument segmentation,” in *ISBI*, 2023.
- [60] T. Chen, L. Zhu, C. Deng, R. Cao, Y. Wang, S. Zhang, Z. Li, L. Sun, Y. Zang, and P. Mao, “Sam-adapter: Adapting segment anything in underperformed scenes,” in *ICCV*, 2023.
- [61] D. R. Muir and S. Sheik, “The road to commercial success for neuromorphic technologies,” *Nature Communications*, 2025.

SUPPLEMENTARY A

SPIKE-DRIVEN VIDEO TRANSFORMER

The backbone video encoder follows a *Conv+ViT* design, a structure demonstrated to provide strong scalability and generalization in both ANNs and SNNs [20]. The overall architecture is illustrated in Fig. 2 and detailed as follows.

Spike-Driven CNN Block integrates a separable convolution module with a subsequent channel-wise convolution module, designed to extract both spatial and inter-channel features effectively. The process can be described as follows

$$\begin{aligned} \mathbf{U}' &= \mathbf{U} + \text{SepConv}(\mathbf{U}), \\ \text{SepConv}(\mathbf{U}) &= \text{Conv}_{\text{pw}}(\text{Conv}_{\text{dw}}(\mathcal{S}\mathcal{N}(\text{Conv}_{\text{pw}}(\mathcal{S}\mathcal{N}(\mathbf{U}))))), \\ \mathbf{U}'' &= \mathbf{U}' + \text{ChannelConv}(\mathbf{U}'), \\ \text{ChannelConv}(\mathbf{U}') &= \text{Conv}(\mathcal{S}\mathcal{N}(\text{Conv}(\mathcal{S}\mathcal{N}(\mathbf{U}')))). \end{aligned} \quad (10)$$

Here, Conv_{pw} , Conv_{dw} and Conv represent point-wise, depth-wise and standard convolutions, respectively.

This block first applies a separable convolution to the input \mathbf{U} , producing an intermediate feature map \mathbf{U}' through a residual connection. To further strengthen inter-channel feature interactions, a channel-wise convolution is then applied to \mathbf{U}' , followed by another residual addition to obtain the output \mathbf{U}'' . Temporal dependencies are implicitly modeled through the inherent spiking dynamics, where neuron membrane potentials integrate incoming signals over time, enabling the network to capture temporal continuity across frames.

Spike-Driven Spatiotemporal Transformer Block integrates spike-driven attention and feedforward modeling to capture rich spatiotemporal dynamics. It consists of a spike-driven joint space-time attention mechanism, followed by a channel-wise MLP for feature refinement. The overall computation is formulated as

$$\begin{aligned} \mathbf{Q}_s, \mathbf{K}_s, \mathbf{V}_s &= \text{Reshape}(\mathcal{S}\mathcal{N}(\text{RepConv}(\mathbf{U}))), \\ \mathbf{U}' &= \mathbf{U} + \text{RepConv}(\text{SDHA}(\mathbf{Q}_s, \mathbf{K}_s, \mathbf{V}_s)), \\ \mathbf{U}'' &= \mathbf{U}' + \text{ChannelMLP}(\mathbf{U}'), \\ \text{ChannelMLP}(\mathbf{U}') &= \text{MLP}(\mathcal{S}\mathcal{N}(\text{MLP}(\mathcal{S}\mathcal{N}(\mathbf{U}')))). \end{aligned} \quad (11)$$

Here, RepConv denotes the re-parameterized convolution. The tensors \mathbf{Q}_s , \mathbf{K}_s , and $\mathbf{V}_s \in 0, 1^{TN \times D}$ represent binary spiking features serving as the query, key, and value, respectively, where TN is the number of spatiotemporal tokens and D is the feature dimension. SDHA denotes the Spike-Driven Hamming Attention, which jointly captures spatial and temporal dependencies, and is defined as

$$\text{SDHA} = \mathcal{S}\mathcal{N}_{2D} \left(\underbrace{(2\mathbf{Q}_s - 1) \left[(2\mathbf{K}_s - 1)^\top \mathbf{V}_s \right]}_{\mathcal{O}(TND^2)} \right). \quad (12)$$

By integrating spiking attention with hierarchical feature transformation, the transformer effectively learns compact yet discriminative spatiotemporal representations optimized for downstream video tasks.

The efficiency of this module is attributed to two core design principles: 1) The transformations $(2\mathbf{Q}_s - 1)$ and $(2\mathbf{K}_s - 1)$ remap binary spike values from $\{0, 1\}$ to $\{-1, 1\}$, which can be implemented using simple bitwise operations, thereby

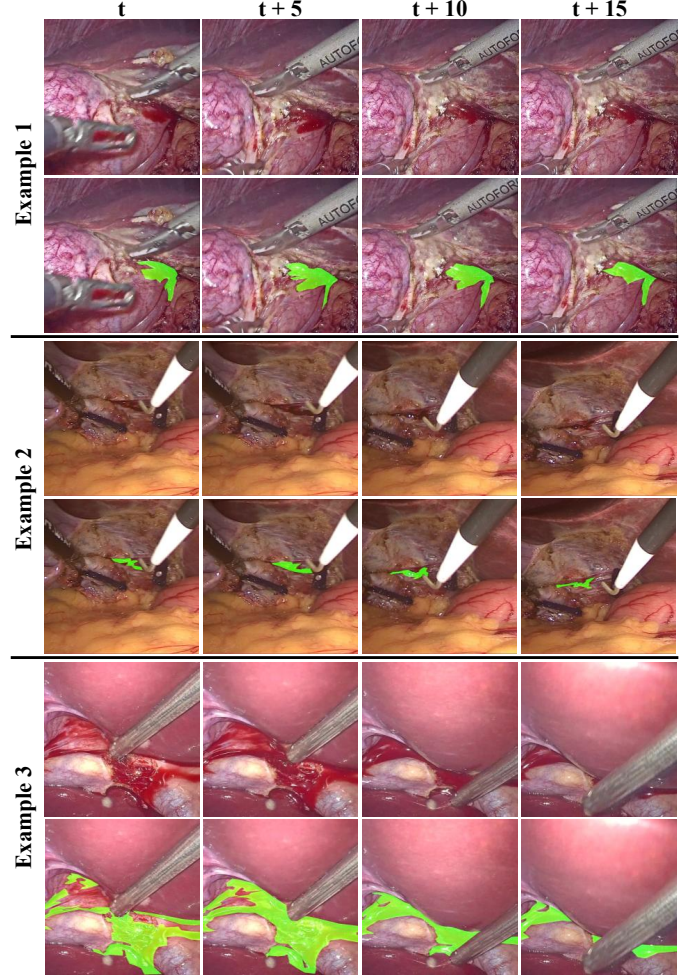


Fig. 9: **Video Clip Examples in SurgBleed Dataset.** The primary challenges in this surgical scene dataset arise from the irregular and highly dynamic bleeding boundaries, *i.e.*, substantial variation in bleeding size and frequent occlusions caused by surgical instruments. Unlike prior EndoVis18 dataset, which focus primarily on instrument segmentation, our in-house dataset is designed to better reflect real-world surgical environments.

avoiding multiplications. Additionally, the scaling factor $\frac{1}{2D}$ can be absorbed into the spiking neuron's threshold, further eliminating the need for multiplications during inference. The matrix multiplication in Eq. (12) can be executed using additions and data addressing techniques. 2) By reordering the computation [14], [20], [26], the complexity of SDHA remains linear with respect to the space-time token length TN , specifically $\mathcal{O}(TND^2)$. In contrast, conventional ANN-based space-time joint attention incurs a much higher cost of $\mathcal{O}(T^2N^2D)$ due to its quadratic dependence on both temporal and spatial dimensions. These properties make SDHA significantly more *efficient* and *scalable* for video-based vision tasks, offering a substantial advantage when processing large-scale video data by greatly reducing computational overhead.

Tab. VI outlines the architecture of the spike-driven video encoder. The network progressively downsamples spatial resolutions while increasing channel dimensions to capture hier-

TABLE VI: **Architecture Details of the Spike-Driven Video Encoder.** For clarity, the temporal spiking layer is omitted here.

† A hidden dimension of 512 (instead of 384) is used to enhance the representational capacity of the small-sized model.

| Blocks | Layers | | Shape | Channel (16M) | Channel (56M) |
|--------|---|--|--|---------------|---------------|
| 1 | DownSample × 1 | Conv (kernel=7x7, stride=2) | $T \times \frac{H}{2} \times \frac{W}{2} \times C$ | 32 | 64 |
| | Spik-Driven CNN Block × 1 | SepConv(kernel=7x7, stride=1) ChannelConv(kernel=3x3, stride=1) | | | |
| | DownSample × 1 | Conv (kernel=3x3, stride=2) | $T \times \frac{H}{4} \times \frac{W}{4} \times 2C$ | 64 | 128 |
| | Spik-Driven CNN Block × 1 | SepConv(kernel=7x7, stride=1) ChannelConv(kernel=3x3, stride=1) | | | |
| 2 | DownSample × 1 | Conv (kernel=3x3, stride=2) | $T \times \frac{H}{8} \times \frac{W}{8} \times 4C$ | 128 | 256 |
| | Spik-Driven CNN Block × 2 | SepConv(kernel=7x7, stride=1) ChannelConv(kernel=3x3, stride=1) | | | |
| 3 | DownSample × 1 | Conv (kernel=3x3, stride=2) | $T \times \frac{H}{16} \times \frac{W}{16} \times 8C$ | 256 | 512 |
| | Spike-Driven Spatiotemporal Transformer × 6 | SDHA(channel=8C) ChannelMLP(ratio=4) | | | |
| 3 | DownSample × 1 | Conv (kernel=3x3, stride=2) | $T \times \frac{H}{16} \times \frac{W}{16} \times 12C$ | 512† | 768 |
| | Spike-Driven Spatiotemporal Transformer × 2 | SDHA(channel=12C) ChannelMLP(ratio=4) | | | |

archical spatiotemporal features. Each stage integrates spike-driven CNN and Transformer blocks to model both local and global dynamics efficiently. The small model uses a hidden dimension of 512 instead of 384 in the 4-th block to enhance representational capacity, ensuring strong performance under compact configurations.

SUPPLEMENTARY B EXAMPLES IN SURGBLEED DATASET

Most existing work on surgical scene understanding is centered on instrument segmentation [6]–[8]. While instruments indeed provide crucial cues for interpreting surgeons’ actions and operational contexts, they represent only one part of the broader surgical scene. Other clinically relevant components, particularly those reflecting intra-operative complications, remain underexplored and insufficiently validated. To bridge this gap, we introduce a new in-house dataset that complements conventional instrument-focused benchmarks by providing pixel-level annotations of bleeding regions for the scenario of intra-operative bleeding alert.

As shown in Fig. 9, the bleeding regions exhibit substantial variations in spatial extent, intensity, and temporal evolution, often accompanied by specular reflections, fluid turbulence, and occlusions from surgical tools. These factors lead to highly non-rigid and temporally inconsistent bleeding boundaries, posing significant challenges for robust segmentation. Unlike existing benchmarks such as EndoVis18 that primarily emphasize instrument segmentation, the SurgBleed dataset focuses on dynamic bleeding localization, highlighting the need for models capable of fine-grained, temporally coherent segmentation under real surgical conditions. The visual examples clearly demonstrate that accurate detection of small and irregular bleeding areas is essential for reliable intra-operative alerting and decision support.